Materials Advances

ROYAL SOCIETY OF CHEMISTRY

PAPER

View Article Online
View Journal | View Issue

Cite this: *Mater. Adv.*, 2025, **6**, 5618

Structural, optical, surface chemical, and electrochemical characterization of Aloe vera-assisted ZnO nanostructures for supercapattery applications

Mohit Bhatt, *[a] Kajal Gautam, [b] Akarsh Verma [c] and A. K. Sinha*[a]

Received 28th May 2025,
Accepted 27th June 2025

DOI: 10.1039/d5ma00556f

rsc.li/materials-advances

Material advancement through green synthesis routes is rapidly gaining attention as a sustainable and scalable alternative for nanomaterial fabrication. In this study, zinc oxide nanostructures (Alv-ZnO NSs) were synthesized using Aloe vera gel as a natural reducing and stabilizing agent, eliminating the need for toxic reagents. This work presents the first comprehensive structural, optical, chemical, and electrochemical investigation of Aloe vera-assisted ZnO nanostructures using advanced characterization techniques, such as XRD, XPS, FESEM, and TEM. Rietveld refinement confirmed high crystallinity and phase purity, while thermal analysis showed excellent thermal stability with only ~2% mass loss up to 750 °C. UV-vis and PL spectroscopy revealed a bandgap of 3.74 ± 0.10 eV and characteristic emissions associated with Zn vacancies and oxygen interstitials, respectively. XPS analysis showed a blue shift in Zn 2p and O 1s peaks, indicating oxygen-rich surfaces and defect sites that contribute to enhanced electrochemical performance. The electrode was characterised by 952.5 F g^{-1} at 1 A g^{-1} and 744.66 F g^{-1} at 1 mV s^{-1}, with 72.9% retention at 10 A g^{-1}, establishing Alv-ZnO NSs as a sustainable, high-performance supercapattery material.

1. Introduction

The rapid depletion of fossil fuel reserves and the adverse environmental consequences associated with their utilization have driven the demand for sustainable energy solutions.[1,2] Green chemistry principles offer a viable approach to mitigating these challenges by emphasizing environmentally benign synthesis methods, reducing hazardous chemical usage, and promoting energy-efficient processes.[3] In this context, the green synthesis of nanomaterials has gained significant interest due to its cost-effectiveness, reduced environmental footprint, and the utilization of renewable resources.[4] Among various green routes, plant extract-assisted synthesis has emerged as a promising alternative, leveraging bioactive compounds, such as polyphenols, flavonoids, and polysaccharides, to facilitate nanoparticle formation while simultaneously enhancing their stability.[5–7] The ever-increasing global energy demand, coupled with the depletion of fossil fuel reserves and their associated environmental ramifications, has necessitated the transition toward sustainable energy alternatives.[8] Renewable energy sources such as solar and wind power offer promising solutions to address these challenges. However, their intermittent nature requires the development of efficient and reliable energy storage systems to bridge the gap between energy generation and consumption.[9] Advanced energy storage technologies, particularly batteries, supercapacitors and supercapatteries (SCs) (mixed: diffusion and surface-controlled mechanism), are pivotal in enabling the large-scale adoption of renewable energy. However, challenges related to material sustainability, cost, and performance optimization persist and demand innovative solutions.[8] Metal oxides have garnered significant attention as active materials in energy storage systems due to their exceptional physicochemical and electrochemical properties.[10] For example, NiO (1358 F g^{-1} at 1 A g^{-1}),[11] RuO_2 (1724 F g^{-1} at 5 A g^{-1}),[12] Co_3O_4 (1015 F g^{-1} at 1 A g^{-1}),[13] and $NiCo_2O_4$ (1254 F g^{-1} at 2 A g^{-1})[14] are remarkable pseudocapacitive materials that offer significantly higher specific capacitance compared to EDLCs. However, their low intrinsic conductivity remains a major limitation, leading to reduced stability. RuO_2, despite its high capacitance, is hindered by its high cost and toxicity, making large-scale SC applications impractical. Hence, the development of cost-effective and high-performance electrode materials remains a crucial area of research for advancing SC technology.

Apart from these, zinc oxide (ZnO) has emerged as a material of interest, owing to its wide bandgap, high ionic conductivity, excellent thermal stability, and structural versatility.[15] Furthermore, ZnO offers a sustainable advantage

[a] *Department of Physics, School of Advanced Engineering, UPES, Dehradun, 248007, India. E-mail: mhtt.mb@gmail.com, anilksinha11@gmail.com*
[b] *Department of Chemistry, School of Advanced Engineering, UPES, Dehradun, 248007, India*
[c] *Department of Mechanical Engineering, School of Advanced Engineering, UPES, Dehradun, 248007, India*

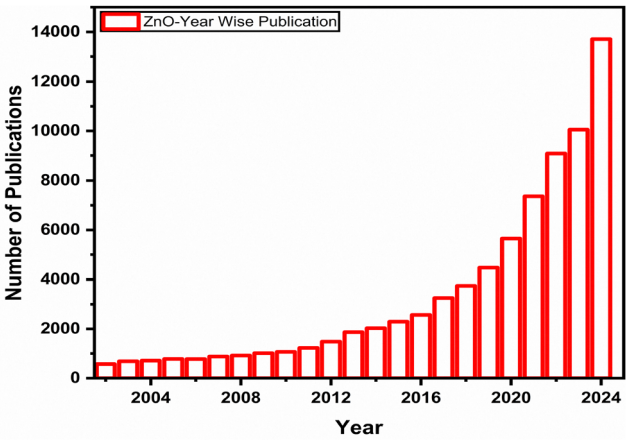

Fig. 1 Trend in research publications highlighting the growing interest in zinc oxide (ZnO) for energy storage applications over recent years. Data sourced from https://ScienceDirect.com.

over materials, such as cobalt, nickel, vanadium, and titanium oxides, which are often limited by high costs, environmental concerns, and restricted availability. Zinc, being abundant, cost-effective, and environmentally benign, positions ZnO as an attractive alternative for energy storage applications, with the added benefit of scalability for industrial applications.[16] A recent trend analysis of research publications on ZnO for energy storage, using data collected from **https://ScienceDirect.com** (shown in Fig. 1), highlights a significant increase in interest over the past few years. This growth underscores the recognition of the potential of ZnO as a key material for next-generation energy storage systems. In comparison to other transition metal oxides, ZnO exhibits superior stability and adaptability, making it particularly suitable for advanced devices.[17] While manganese and vanadium oxides are promising, their moderate stability and processing complexities can limit their widespread application. Similarly, cobalt and titanium oxides, despite their excellent electrochemical properties, are constrained by their high production costs and limited global availability.[18] ZnO thus offers a balanced solution by combining affordability, sustainability, and high performance.

Various methods, such as hydrothermal, sol–gel, and co-precipitation techniques, are commonly used for nanomaterial synthesis. However, these methods often involve high costs and the use of toxic chemicals, which pose environmental and safety concerns.[19–21] To address these issues, green synthesis has emerged as a sustainable alternative for producing nanoparticles (NPs) using plant extracts, enzymes, or microorganisms. This approach is increasingly favoured due to its cost-effectiveness, safety, rapid process, and eco-friendly nature.[5] Plant extracts, in particular, have drawn significant attention for nanoparticle synthesis because of their availability, efficiency, and green attributes. These extracts contain natural antioxidants, such as amino acids, polyphenols, reducing sugars, and nitrogenous bases, which act as both reducing and capping agents.[3,5,22] These compounds facilitate the reduction of metal ions while stabilizing nanoparticles, preventing their agglomeration. Additionally, plant structures act as bio-templates to control particle size and morphology.[3] While several studies have recently reported the green synthesis of undoped and doped ZnO nanoparticles as well as their heterostructures, using different plant extracts, such as *Justicia adhatoda*,[23] *Elettaria cardamomum*,[24] Sansevieria Trifasciata roots,[25] Lognata leaves,[26] and Aloe-vera,[27] for photocatalytic, dye degradation, energy storage, antimicrobial and other medical applications. The focus of these research works has largely remained limited to environmental remediation and applications. In this paper, we study the reasons for the superior specific capacitance of Aloe-vera assisted ZnO nanoparticles using optical (photoluminescence) and XPS characterization.

In this study we have synthesised Alv-ZnO NSs using a one step green synthesis method, in which Aloe vera gel extract was employed as a natural reducing and capping agent to synthesize Alv-ZnO NSs through a green synthesis approach. The bioactive compounds in Aloe vera, including polysaccharides, phenolics, and flavonoids, facilitated the reduction of zinc precursors while enhancing the stability of the synthesized nanoparticles.[3] The electrochemical analysis indicates an exceptional specific capacitance of 952.5 F g^{-1} at 1 A g^{-1} and an impressive 744.66 F g^{-1} at 1 mV s^{-1}, surpassing previously reported values for ZnO-based electrodes (as shown in Table 1). While several ZnO-based hybrid composites often demonstrate higher specific capacitance, due to improved conductivity,[28–38] their fabrication typically involves conventional chemical methods that compromise the green and sustainable nature of synthesis. Therefore, in the context of eco-friendly materials design, the performance of our Aloe vera-assisted ZnO nanostructures represents a promising and cleaner alternative. Beyond high capacitance, this study presents several quantifiable advancements over existing literature specifically on Aloe vera-assisted green-synthesized ZnO, distinguishing it from studies using other conventional methods. Structural and defect-level characterizations *via* PL and XPS confirm the presence of Zn vacancies and oxygen interstitials, defect sites that directly contribute to better electrochemical activity. Rietveld refinement further verifies phase purity and nanoscale crystallinity, while TGA demonstrates excellent thermal stability with only ~2% mass loss up to 750 °C. By integrating crystallographic, optical, surface chemical, and electrochemical data, this work establishes a robust structure–property–performance correlation. These findings highlight the effectiveness of Aloe vera-assisted green synthesis in producing Alv-ZnO NSs with improved stability and superior electrochemical performance, making them promising candidates for SC applications. Moreover, the significant improvement in capacitance makes them a more efficient alternative to conventionally synthesized ZnO-based materials.

2. Experimental section

2.1 Characterization techniques

The characterization of Alv-ZnO NSs was performed using various advanced techniques. X-Ray diffraction (XRD) was utilized to examine the crystalline structure and confirm the phase purity of the ZnO material. Fourier-transform infrared spectroscopy (FTIR) was employed to identify functional groups

Table 1 Comparison of electrochemical performance of Alv-ZnO NSs with other ZnO-based electrodes

Material	Synthesis	Specific capacitance	Ref.
Alv-ZnO NSs	Green synthesis	952.5 F g^{-1} at 1 A g^{-1} and 744.66 F g^{-1} at 1 mV s^{-1}	This work
ZnO–rGO	Green synthesis	535 F g^{-1} at 1 A g^{-1}	39
ZnO nanocomposites	Green synthesis	820 F g^{-1} at 1 A g^{-1}	40
ZnO nanocomposite	Green synthesis	268.5 A g^{-1} at 0.1 A g^{-1}	41
ZnO–GO nanocomposite	Green synthesis	523.4 F g^{-1} at 2 A g^{-1}	42
ZnO nanoparticles	Green synthesis	667 F g^{-1} at 1 A g^{-1}	43
ZnO–Ag nanocomposite	Green synthesis	189.52 F g^{-1} at 0.5 A g^{-1}	44
ZnO@rGO	Green synthesis	303 F g^{-1} at 10 A g^{-1}	45
ZnO/graphene	Green synthesis	236 F g^{-1} at 10 A g^{-1}	46
ZnO–carbon nanosphere	Facile low-temperature water-bath	630 F g^{-1} at 2 A g^{-1}	47
ZnO–carbon nanotubes	Spray pyrolyser	324 F g^{-1} at 1 A g^{-1}	48
ZnO/carbon aerogel nanocomposite	Co-precipitation	500 F g^{-1} at 1 A g^{-1}	49
ZnO-activated carbon	Sol gel	160 F g^{-1} at 1 A g^{-1}	50
ZnO nanocomposite	Co-precipitation	375 F g^{-1} at 75 mA cm^{-2}	51
ZnO nanopowder	Hydrothermal	448 F g^{-1} at 0.25 A g^{-1}	52
ZnO nanocomposite	Solvothermal	122.4 F g^{-1} at 5 mV s^{-1}	53
ZnO nanorods	Hydrothermal	867 mF cm^{-2} at 2 mA cm^{-2}	54
ZnO nanorods	Wet chemical	370 F g^{-1} at 10 A g^{-1}	55
ZnO nanopetals	Spray pyrolysis	365 F g^{-1} at 5 mV s^{-1}	56
ZnO nanoparticles	Hydrothermal	330 F g^{-1} at 0.1C	57

and detect Aloe vera-derived bioactive compounds in the synthesized material. Field emission scanning electron microscopy (FESEM) was used to analyse the particle morphology, while energy-dispersive X-ray spectroscopy (EDX) was employed to evaluate the elemental composition. Transmission electron microscopy (TEM) was carried out for detailed insights into particle size and lattice fringes. Additionally, X-ray photoelectron spectroscopy (XPS) was employed to investigate the elemental composition and oxidation states, and UV-vis spectroscopy and PL spectra were used to study the optical properties, including the bandgap of the synthesized Alv-ZnO NSs.

2.2 Synthesis of ZnO nanostructures (Alv-ZnO NSs)

Fresh Aloe vera leaves were sourced from the polyhouse at UPES, Dehradun, India. The leaves were thoroughly washed with double deionized (DDI) water multiple times to remove dust and impurities. Approximately 20 g of gel was extracted from the cleaned leaves and transferred into a beaker. The gel was then blended with 100 mL of DI water using a cleaned grinder mixer to obtain a fine, viscous mixture. This mixture was heated in a hot air oven at 85 °C for 2 h to achieve a uniform solution. Zinc acetate monohydrate $Zn(CH_3COO)_2{\cdot}H_2O$) (10 g) was dissolved in as prepared Aloe vera gel under continuous stirring. The prepared Aloe vera gel acted as a natural reducing agent. The resulting mixture was stirred at 80 °C for 1–2 h until a dark, viscous gel was formed. This gel was subsequently calcined in a muffle furnace at 400 °C for 2.5 h with a ramp rate of 5 °C min^{-1}, yielding Alv-ZnO NSs. The synthesis procedure has been shown in Fig. 2.

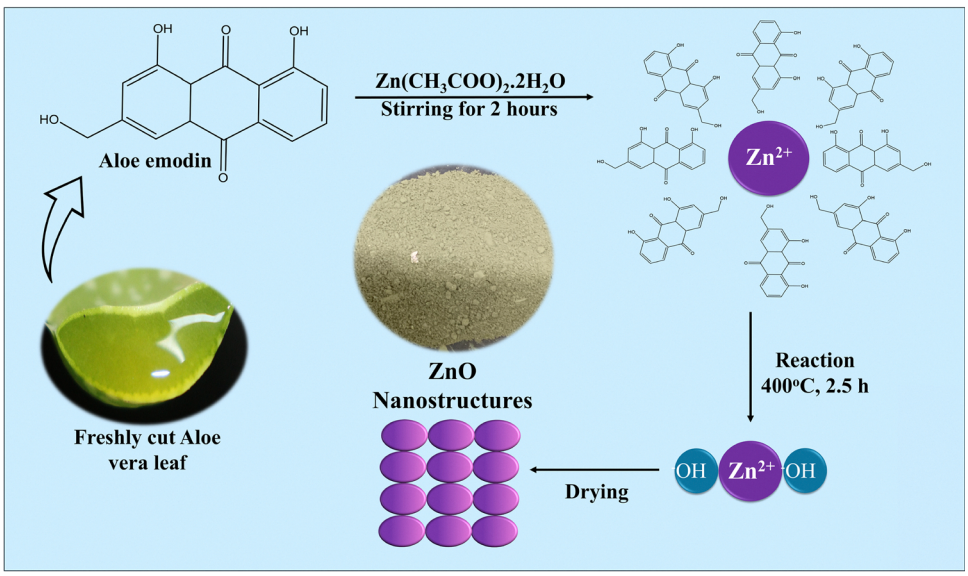

Fig. 2 Schematic of formation of ZnO nanoparticles using Aloe vera gel (created with https://biorender.com).

2.3 Reaction mechanism of Alv-ZnO NSs

Hydrolysis of zinc acetate. Zinc acetate monohydrate $Zn(CH_3COO)_2{\cdot}H_2O$ dissolves in Aloe vera gel solution, and upon heating, it undergoes hydrolysis to form zinc hydroxide ($Zn(OH)_2$):

$$Zn(CH_3COO)_2{\cdot}H_2O + H_2O \rightarrow Zn(OH)_2 + 2CH_3COOH$$

Reduction by Aloe vera gel. The bioactive compounds in Aloe vera gel (such as polysaccharides, phenolics, and flavonoids) act as reducing agents, facilitating the reduction of zinc ions (Zn^{2+}) to $Zn(OH)_2$

$$Zn^{2+} + 2\text{Aloe vera compounds} \rightarrow Zn(OH)_2 + \text{Aloe vera compounds (oxidized)}$$

Aloe vera compounds help stabilize the formed zinc hydroxide by preventing agglomeration, ensuring uniform nanoparticle formation.

Calcination to form Alv-ZnO NSs. Upon heating the gel mixture at 400 °C, the zinc hydroxide undergoes dehydration and transformation into ZnO, with water being released:

$$Zn(OH)_2 \rightarrow ZnO + H_2O$$

Overall reaction. The overall reaction (eqn (1)) for the formation of ZnO NSs from zinc acetate monohydrate and Aloe vera gel extract is:

$$Zn(CH_3COO)_2{\cdot}H_2O + 2H_2O + \text{Aloe vera gel} \rightarrow ZnO + 2CH_3COOH + H_2O \quad (1)$$

2.4 Electrochemical characterization

To fabricate the working electrode, a slurry was prepared by mixing the active material, conductive carbon black, and polyvinylidene fluoride (PVDF) in a weight ratio of 8 : 1 : 1. Carbon black was incorporated to enhance the electrical conductivity of the electrode, while PVDF served as a binding agent to ensure mechanical stability. The mixture was dissolved in *N*-methyl-2-pyrrolidone (NMP) to form a homogenous slurry, which was uniformly coated onto a pre-cleaned nickel foam substrate (1 × 1 cm^2). The nickel foam was cleaned following the procedure reported in the literature,[58] ensuring the removal of any surface impurities. The coated nickel foam was then dried in a vacuum oven at 80 °C for 12 h to remove residual solvent. The prepared electrode was used as the working electrode in a three-electrode configuration, with platinum foil (2 × 2 cm^2) serving as the counter electrode and a saturated calomel electrode (SCE) as the reference electrode.

Cyclic voltammetry (CV) was conducted to evaluate the redox activity of the material and determine the anodic and cathodic peak current responses at varying scan rates. The CV data were analysed using the power-law equation (eqn (4)) to distinguish between diffusion-controlled and capacitive contributions to the charge storage mechanism. Galvanostatic charge–discharge (GCD) measurements were performed to determine the specific capacitance of the material, enabling the assessment of its energy storage performance. Electrochemical impedance spectroscopy (EIS) was employed to study the charge transfer resistance and ion diffusion behavior of the electrode material across a frequency range of 10 mHz to 100 kHz. The Nyquist plots obtained from EIS provided insights into the conductivity and interfacial charge transport characteristics of the material, which are critical for evaluating its suitability for energy storage applications.

3. Results and discussion

The structural and phase analysis of the Alv-ZnO NSs were investigated using X-ray diffraction (XRD) techniques. In Fig. 3(a) is the experimental XRD pattern along with the theoretical pattern calculated using Rietveld refinement. Also shown in the figure is the difference ($I_{Experimental} - I_{Theorotical}$) pattern. The Rietveld refinement was done using Fulprof software.[59] The excellent goodness of fit ($\chi^2 = 2.276$) confirms the high crystalline quality of the material. The diffraction peaks correspond to the hexagonal wurtzite structure of ZnO,[3] and no secondary phases or impurity peaks were observed, indicating the successful synthesis of pure Alv-ZnO NSs. The refined structural parameters, such as the space group (*P*63*mc*), lattice constants, and other crystallographic details, are consistent with the standard wurtzite structure.

The lattice parameters were determined as $a = b = 3.25$ Å, $c = 5.21$ Å, with interaxial angles of $\alpha = \beta = 90°$: $\gamma = 120°$. These precise values align with the standard hexagonal wurtzite structure of ZnO, which are in good agreement with standard ZnO (JCPDS no. 36-1451), and these results align well with the values reported in the literature,[60] further verifying the structural integrity and purity of the synthesized Alv-ZnO NSs. To evaluate the microstructural characteristics, crystallite size and strain factor were calculated using the Rietveld refinement parameters, as shown in Fig. 3(b). The average crystallite size, indicative of the grain size, falls within the nanoscale range, *i.e.* 41.7 ± 0.2 nm, ensuring a high surface area that is beneficial for energy storage applications. The micro-strain estimated using the size-strain (SSP) method was estimated as 1.36%, reflecting high lattice distortions, probably due to the intrinsic defects. These results underline the precise synthesis process and the high-quality nature of the Alv-ZnO NSs. The thermal stability of the Alv-ZnO NSs was evaluated using thermogravimetric analysis (TGA). As shown in Fig. 3(c), the TGA curve shows exceptional thermal stability, with only a minor weight loss of approximately 2% observed up to 750 °C, which is much lower compared to the ZnO nanomaterial reported.[61,62] This negligible weight loss can be attributed to the evaporation of residual organic compounds and adsorbed water.[63–66] Beyond this, the material exhibits no significant decomposition or phase change underscoring its robust thermal resistance. The excellent thermal stability observed in TGA further complements the structural findings from XRD. The absence of phase transitions or material degradation at elevated temperatures reinforces the suitability of these Alv-ZnO NSs for applications that demand high-temperature stability, such as in supercapacitors, batteries,

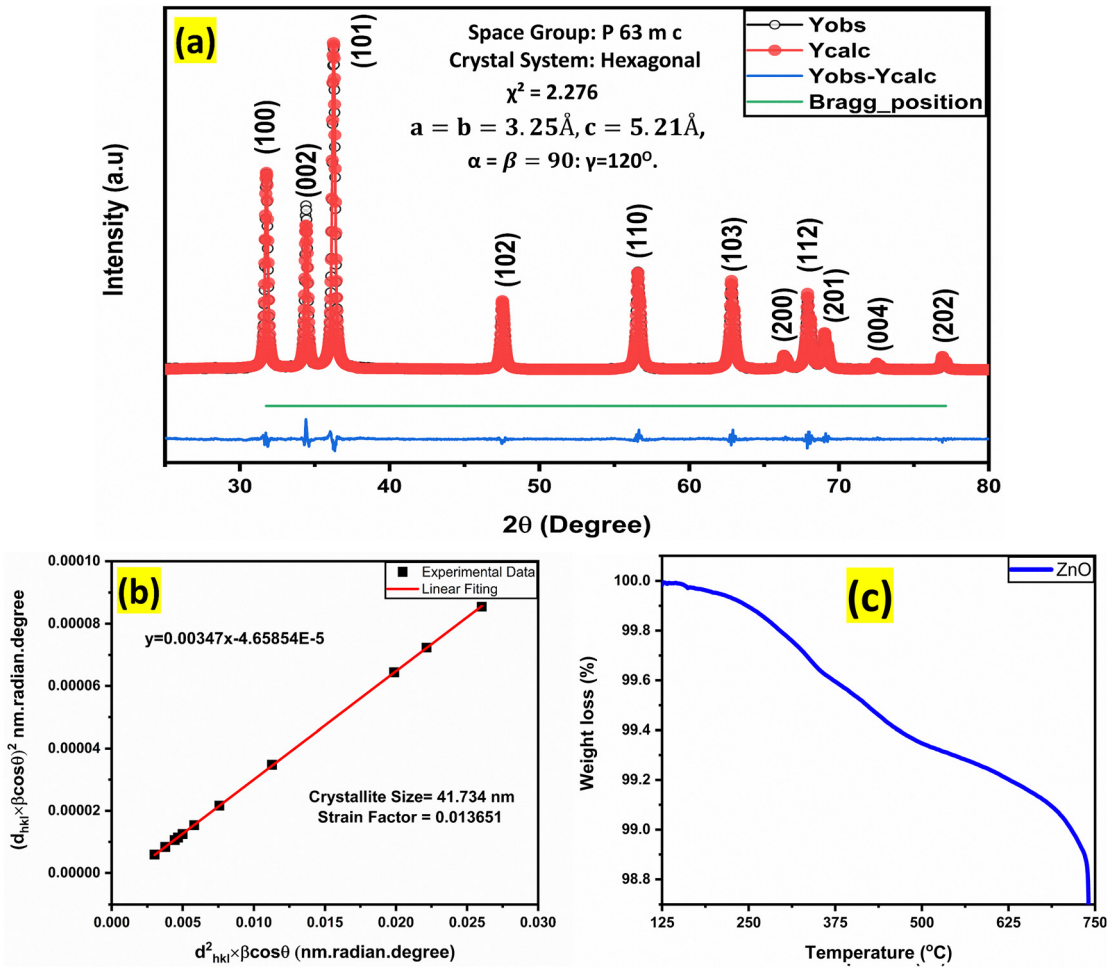

Fig. 3 (a) Rietveld refinement of the Alv-ZnO NS XRD data for the crystal lattice constants, (b) SSP plot showing crystallite size and strain, and (c) TGA curve indicating ~2% mass loss, verifying high stability.

photocatalysis, and gas sensors.[67,68] The synergistic insights from XRD and TGA highlight the superior quality and potential of the synthesized Alv-ZnO NSs for SC applications.

The FTIR spectrum of Aloe vera (red curve in Fig. 4) shows a broad O–H stretching band (3560–3200 cm^{-1}, centered at ~3366 cm^{-1}), attributed to phenolic compounds and carboxylic acids such as aloin and emodin.[22,69] Distinct C–H stretching bands at ~2919 and 2853 cm^{-1}, and peaks near 1415 cm^{-1} (symmetric carboxylate stretching), 1254 cm^{-1} (C–O–C in *O*-acetyl esters), and 1099 cm^{-1} (C–O/C–OH from glucan units in polysaccharides) are also observed.[22] These assignments are consistent with our previously reported data and existing literature.[22] In comparison, the Alv-ZnO spectrum (black curve in Fig. 4) exhibits attenuated but noticeable peaks at 3464 cm^{-1} (O–H), 2935 cm^{-1} (C–H), and around 1000–1100 cm^{-1}, alongside a distinct Zn–O stretching region below 600 cm^{-1}.[70,71] The significant weakening of organic-related peaks after calcination at 400 °C suggests that the bulk Aloe vera organics are removed, while a small fraction of surface-bound functional groups remains. These remaining groups likely promote enhanced electrochemical properties by improving electrolyte interaction and wettability. Thus, the inclusion of Aloe vera FTIR data clarifies that the observed bands in the Alv-ZnO spectrum

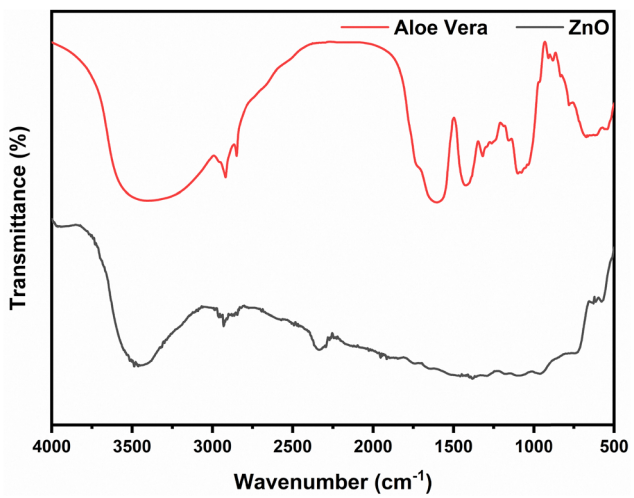

Fig. 4 FTIR spectrum of Aloe vera and Alv-ZnO NSs.

originate from Aloe vera-derived surface functionalization rather than post-calcination environmental adsorption. This directly supports the green synthesis pathway and strengthens the role of Aloe vera in functionalizing ZnO nanostructures.

These observations align with previous studies where Aloe vera extracts have been reported to facilitate the synthesis of ZnO NSs by serving as both reducing and capping agents.[70,72] The presence of functional groups such as hydroxyls, amines, and carboxylates in Aloe vera suggests their active role in ZnO NS formation and stabilization. Moreover, the weak band at 1628 cm^{-1}, corresponding to amide bonds, suggests protein involvement in nanoparticle synthesis, further supporting the biological synthesis mechanism.[72]

The UV absorption spectra of Alv-ZnO NSs, presented in Fig. 5(a), span a range of 200–800 nm. An absorption edge was observed near 380 nm, confirming the presence of highly crystalline ZnO nanostructures.[73] Additionally, a distinct peak at 380 nm was noted, attributed to the surface plasmon resonance (SPR) of the ZnO nanostructures.[74] The presence of SPR in Alv-ZnO NSs enhances charge transfer, improving electrochemical performance and making them promising for energy storage applications such as batteries and SCs. According to Chandran *et al.* ZnO nanoparticles typically exhibit absorption peaks within the 350–400 nm range.[74] A redshift toward longer wavelengths was observed with increasing particle size, further supporting the successful synthesis of ZnO NSs using Aloe vera extract as a reducing agent.[3] The direct optical band gap (E_g) of the synthesized sample was determined using Tauc's equation mentioned in eqn (2), as follows:[73,75]

$$(\alpha h\nu)^2 = A(h\nu - E_g) \quad (2)$$

where A is constant, α represents the optical absorption coefficient, and $h\nu$ is the photon energy.

The estimated E_g was found to be 3.74 ± 0.10 eV. The bandgap of bulk ZnO is 3.37 eV. However, the reported bandgap of the ZnO nanoparticles varies between 3.2 and 3.8 eV, depending on the synthesis method, particle size, morphology, and defects, such as surface defects and oxygen vacancies.[79–81] The E_g value obtained in this study closely matches the 3.8 eV reported by Nabil *et al.*[82] for Alv-ZnO NSs with an average particle size of ~45 nm, synthesized *via* the wet chemical technique. Notably, the average particle size obtained from XRD peak analysis for our sample is ~40 nm.

The bandgap and defect states were analysed using PL spectroscopy. In Fig. 5(b) is the PL emission spectrum, with

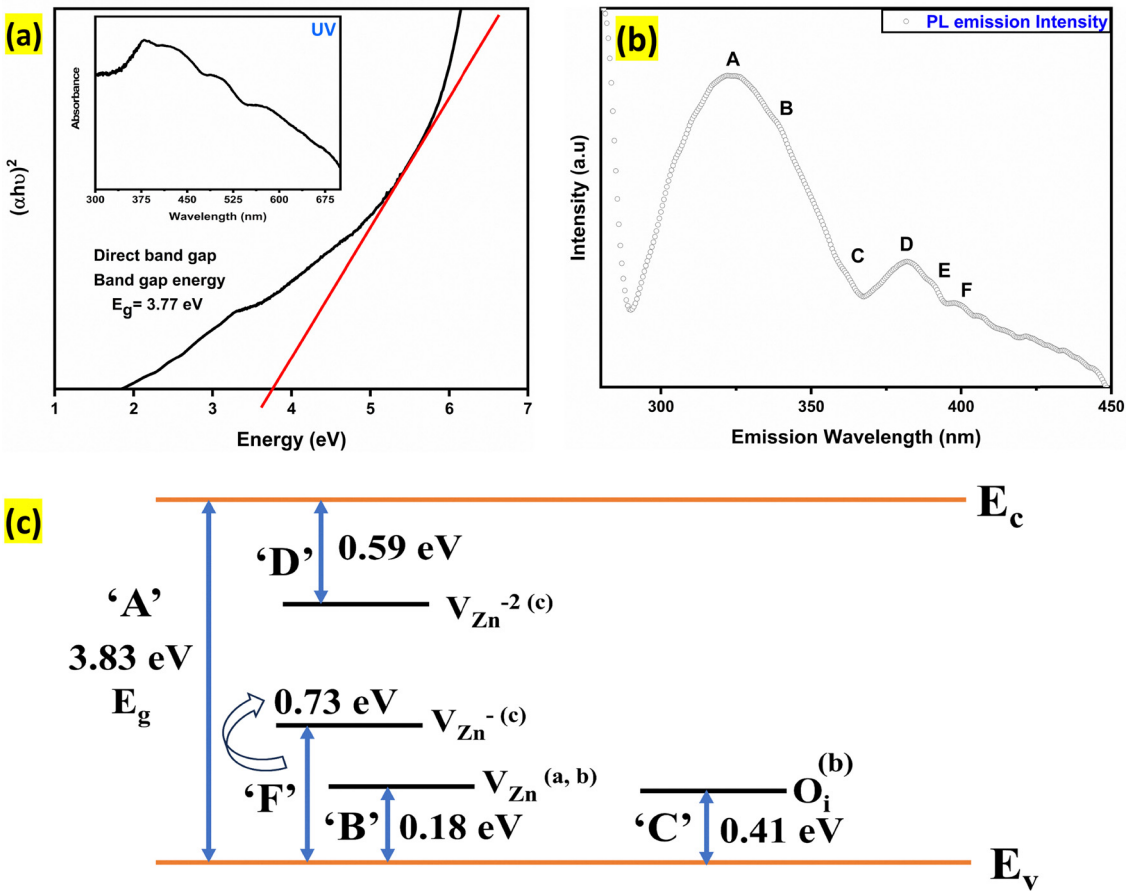

Fig. 5 (a) UV-vis spectroscopy providing the energy band gap, (b) PL spectra of Alv-ZnO NSs, (c) assignment of defect levels observed in the PL spectrum based on first principle calculations, references marked with subscript 'a', 'b' and 'c' are ref. 76–78, respectively. 'A' to 'F' are transitions marked in the PL spectrum (Fig. 5(b)).

emission peaks labelled as 'A' (324 nm = 3.83 eV), 'B' (3.65 eV), 'C' (3.42 eV), 'D' (3.24 eV), 'E' (3.16 eV), and 'F' (3.10 eV). The major emission peak 'A' at 3.83 eV, corresponds to transition from the valence band (VB) to the conduction band (CB), while the other minor peaks arise from transitions between localized defect states and extended states (VB or CB). The defect state assignments, shown in Fig. 5(c), are based on first-principles calculations.[76,78,83] PL spectroscopy analysis clearly reveals that zinc vacancies and oxygen interstitials are present in the ZnO samples synthesized *via* the green synthesis process using Aloe vera. These defect centers play a crucial role in the performance of the material as an electrode for supercapacitors, as they serve as active sites for charge storage.[84] The excellent thermal and chemical stability of the material are crucial for energy storage applications. High band gap suggests favourable dielectric properties, promoting efficient charge separation and storage.[85] A higher value of the energy band gap is attributed to the presence of intrinsic defects like Zn vacancies and oxygen interstitials.[86] Moreover, the presence of abundant surface-active sites enhances redox reactions, positioning Alv-ZnO NSs as a promising candidate for supercapattery behaviour in high-performance SCs.

The defect state-related transitions in the PL spectrum indicate the presence of intrinsic defects like Zn vacancies and oxygen interstitials. To further verify the surface defect configuration, XPS spectra were recorded. In Fig. 6(a) is the survey scan showing the presence of Zn, O and C core levels. The detailed scan at the C 1s core level is shown in Fig. 6(b). The complex spectrum is fitted with three Gaussian peaks positioned at 286.5, 288.2 and 291.1 eV, attributed to adventitious C–C, C═O and O–C═C bonds, respectively.[87,88] The adventitious carbon peak is often used to compensate for the charging effect, especially for insulator samples. Thus, the most intense component observed in the C 1s band is adjusted to a binding energy of 284.8 eV.[89] We observe a blue shift of 1.7 eV in the adventitious peak and hence provide a shift of −1.7 eV in the Zn 2p and O 1s spectra to be discussed below. The other carbon peaks corresponding to C═O and O–C═C are actually at 286.5 eV and 289.4 eV, respectively, after the correction for the charging effect and are in agreement with the literature.[87] The Zn 2p doublet is shown in Fig. 6(c) after Shirley background subtraction and after shifting the spectrum by 1.7 eV to lower the binding energies. The spectrum is fitted with four Gaussian peaks at 1023.2 eV, 1041.2 eV, 1046.3 eV and a broad peak at 1066.6 eV. The first peak at 1023.2 eV represents the Zn $2p_{3/2}$ component and the second peak at 1041.2 eV is the shake-up satellite.[90] A difference of 18.0 ± 0.2 eV between the Zn $2p_{3/2}$ peak and its corresponding satellite peak is in agreement with

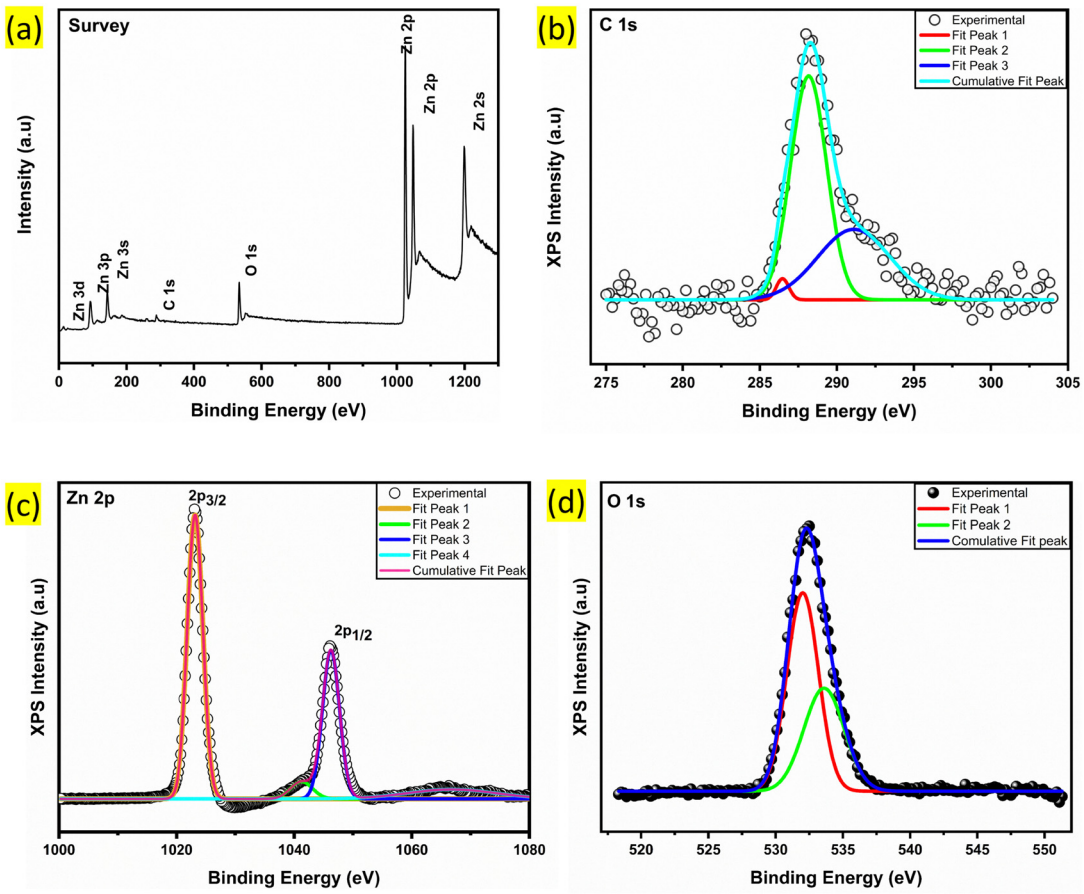

Fig. 6 XPS analysis of Alv-ZnO NSs: (a) survey spectrum, (b) high-resolution C 1s spectrum, (c) Zn 2p spectrum, and (d) O 1s spectrum.

values reported in the literature for ZnO.[91] The third peak at 1046.3 eV is attributed to the Zn $2p_{1/2}$ component and it is positioned at 23.1 eV from the Zn $2p_{3/2}$ peak. This is spin–orbit splitting of the Zn 2p orbital, in agreement with the literature[91–93] and is typical of the Zn^{2+} oxidation state. However, the binding energies of the Zn $2p_{3/2}$ and $2p_{1/2}$ components are found to be blue shifted by about 1 eV in our sample compared to those reported in the literature.[91–93] The blue shift clearly represents that the oxidation state of Zn is more than +2, which may be due to Zn vacancies and/or oxygen interstitials. This also agrees with the PL emission, where the surface defect related emission at 0.18 eV, 0.59 eV and 0.73 eV is attributed to Zn vacancy related defect states (see Fig. 5(c)). Therefore, it can be concluded that Alv-ZnO NSs grown through a green synthesis route contain intrinsic defects in the form of Zn vacancies and/or oxygen interstitials, which may be beneficial for its application as an electrode material for energy storage. In Fig. 6(d), the O 1s core level spectrum of the ZnO sample, after background subtraction, is shown. Two Gaussian peaks are observed at binding energies of 532.0 eV and 533.6 eV. The peak at 533.6 eV is attributed to surface species such as C═O groups,[87,94] while the 532.0 eV peak has often been associated with surface hydroxyl groups (OH).[91,94,95] However, the BE difference between Zn $2p_{3/2}$ (1023.2 eV) and this O 1s component (532.0 eV) is 491.2 eV, which closely matches the BE difference (491.3 eV) observed for lattice oxygen in

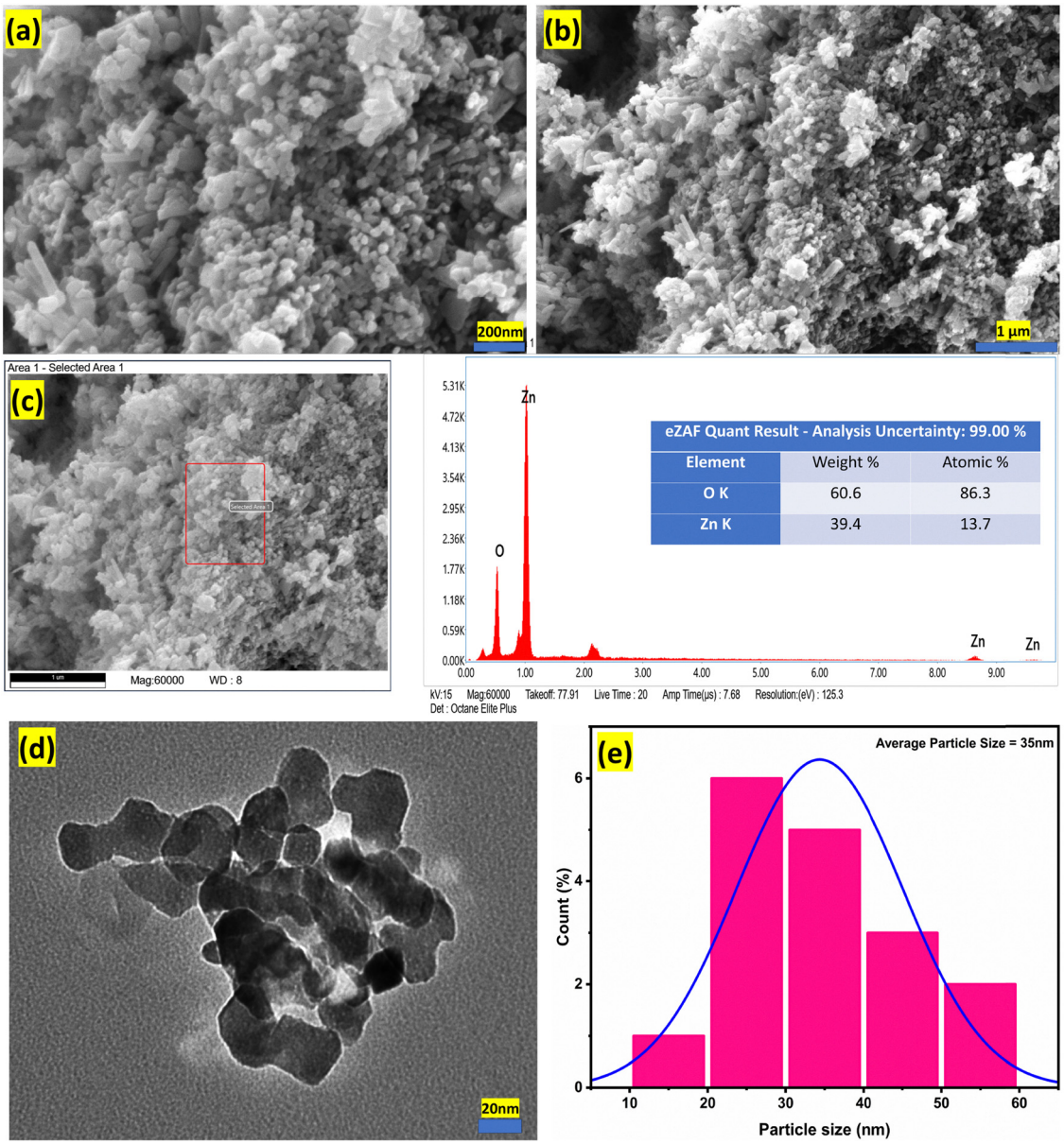

Fig. 7 (a) FESEM images of Alv-ZnO NSs at different magnifications, highlighting their morphology. (b) EDX spectrum confirming the elemental composition and purity of the synthesized Alv-ZnO NSs. (c) EDX analysis. (d) TEM image showcasing the nanoscale features of Alv-ZnO NSs. (e) Histogram from TEM analysis, indicating an average particle size of approximately 35 nm.

single-crystal $ZnWO_4$.[96] This strongly supports the attribution of the 532.0 eV peak to lattice oxygen in ZnO.[97,98]

The FESEM images of Alv-ZnO NSs (as shown in Fig. 7) synthesized using Aloe vera extract reveal a distinctive needle-like morphology with a mesoporous arrangement of nano and submicron particles. The FESEM image shows variations in shape and size of the particles. At higher magnification (Fig. 7(a)), the structures appear as tightly packed and elongated nanoneedles with uniform dimensions, measuring approximately 56 nm in length, 42 nm in width, and 360 nm in height. These needle-like formations exhibit significant porosity and interconnectedness, which are critical for applications requiring high surface area and efficient charge transfer. The lower-magnification images (Fig. 7(b)) provide a broader perspective, showing a dense, three-dimensional network of Alv-ZnO NSs, which further enhances their potential for energy storage applications by improving electrolyte accessibility and ion diffusion pathways. The needle-like morphology of ZnO synthesized through the green route using Aloe vera extract plays a crucial role in energy storage applications. This unique structure provides a high surface area, enhancing the interaction with electrolytes and facilitating charge storage. Additionally, the interconnected structure facilitates rapid ion transport, making these nanostructures highly suitable for SCs and battery electrodes. The use of Aloe vera extract as a sustainable and eco-friendly reducing and capping agent further emphasizes the green synthesis approach, aligning with the global drive toward environmentally conscious material production.

The EDX analysis supports the successful formation of Alv-ZnO NSs, with the elemental composition dominated by zinc (Zn) and oxygen (O), as indicated by their respective peaks in the spectrum. Quantitative data confirm that the weight percentage of oxygen is 60.6%, while zinc accounts for 39.4%. The atomic percentages of oxygen and zinc, 86.3% and 13.7%, respectively, suggest an oxygen-rich ZnO surface, as shown in Fig. 7(c), due to adsorbed species, which is consistent with the expected chemical structure. In Fig. 7(d) is the TEM image of the Alv-ZnO NSs, revealing their well-defined morphology and nanoscale features. The corresponding particle size distribution is shown in Fig. 7(e), where the histogram analysis indicates an average particle size of approximately 35 nm, which is in good agreement with the average crystallite size estimated using XRD peak analysis. These results also complement the FESEM

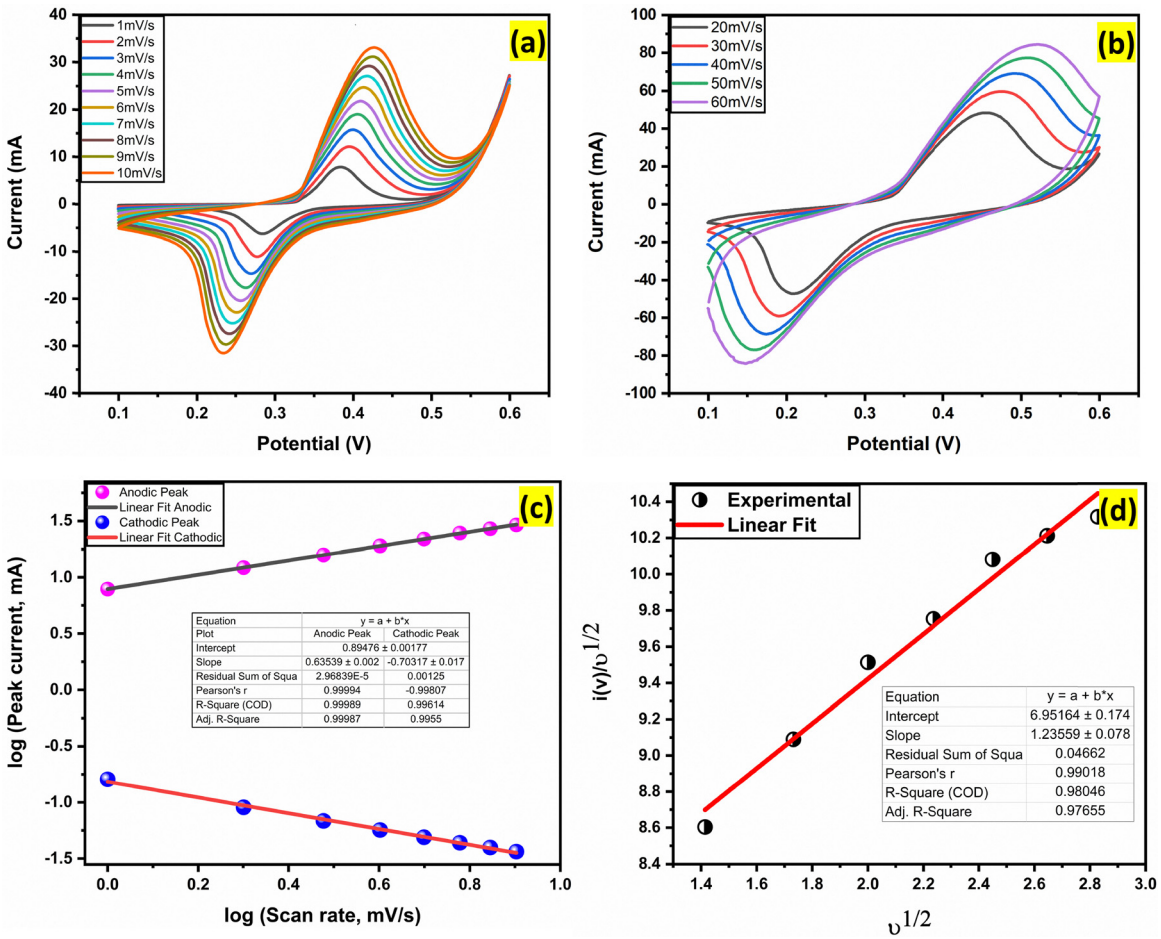

Fig. 8 (a) and (b) Cyclic voltammetry (CV) curves of Alv-ZnO NSs at various scan rates. The specific capacitance was calculated using eqn (9), where m is the mass of active material (1.5 mg), (c) anodic and cathodic peaks and (d) plot of $i(V)/v^{1/2}$ *vs.* $v^{1/2}$ (where v is scan rate).

findings, confirming the nanoscale dimensions of the synthesized Alv-ZnO NSs.

The electrochemical performance of the Alv-ZnO NSs was evaluated using cyclic voltammetry (CV), galvanostatic charge–discharge (GCD), and electrochemical impedance spectroscopy (EIS) in a three-electrode configuration with 2 M KOH as the electrolyte. The measurements were conducted within a potential window of 0.5 V. The CV analysis was performed over a wide scan range from 1 to 60 mV s^{-1}, as shown in Fig. 8(a) and (b). At lower scan rates, the CV profiles (Fig. 8(a)) exhibit well-defined redox peaks, which indicate the pseudocapacitive nature of the material, primarily due to surface-controlled redox reactions. As the scan rate increases (Fig. 8(b)), a broadening of the peaks is observed, which further confirms the pseudocapacitive characteristics of the material. The persistence of distinct oxidation and reduction peaks even at high scan rates indicates that the Alv-ZnO NSs exhibit fast redox kinetics and high reversibility, which can be attributed to their nanostructured morphology.

Aloe vera plays a critical role in the synthesis by acting as a biocompatible and eco-friendly reducing agent, which not only facilitates the formation of Alv-ZnO NSs but also enhances their surface properties.[3,63] This is supported by energy-dispersive X-ray spectroscopy (EDX) analysis, which reveals a high oxygen content of approximately 83% in the Alv-ZnO NSs. The PL data also shows the defect peaks corresponding to oxygen interstitials and Zn vacancies (see Fig. 5(b) and (c)). The abundant oxygen presence is indicative of the high degree of surface oxidation, which could be attributed to the functional groups contributed by Aloe vera during the synthesis process. These oxygen-rich functional groups are likely to enhance the pseudocapacitive behaviour by promoting better interaction between the electrolyte ions and the electrode surface, leading to improved charge storage capability. In addition, interstitial oxygen contributes to improving electronic conductivity.[79,86] The biogenic nature of Aloe vera may aid in creating a more porous and uniformly distributed nanostructure, further facilitating ion transport and redox reactions.[3,5]

The shift of the redox peaks towards more positive and negative potentials at higher scan rates suggests a diffusion-controlled process.[58,99] This shift indicates that, as the scan rate increases, ion diffusion within the electrolyte and electrode interface plays a significant role in the charge storage process.[58,100]

To further understand the charge storage mechanism, the relationship between the peak current (i_p) and the scan rate (v) was analysed using the power law in eqn (4):[100]

$$i_p = av^b \quad (4)$$

where a is a constant, v is the scan rate, and the exponent b determines the nature of the charge storage process. The value of $b = 1$ represents ideal capacitive behaviour, while the a value of 0.5 corresponds to diffusion-controlled, battery-like behaviour.[58,100] For the Alv-ZnO NSs, the calculated b-value for the anodic peak was 0.63 (Fig. 8(c)), confirming the supercapattery mechanism that contains both diffusion and surface-controlled behaviours.

Additionally, the capacitive and diffusion contributions to the total current were separated using eqn (5):[99]

$$i(V) = k_1v + k_2v^{1/2} = I_{\text{capacitive}} + I_{\text{diffusion}} \quad (5)$$

where k_1v represents the capacitive current contribution, and $k_2v^{1/2}$ corresponds to the diffusion-controlled current. By rearranging this eqn (6):[99]

$$\frac{i(V)}{v^{\frac{1}{2}}} = k_1v^{1/2} + k_2 \quad (6)$$

The slope (k_1) and intercept (k_2) of the plot of $\frac{i_p}{v^{\frac{1}{2}}}$ *versus* $v^{1/2}$ (Fig. 4(d)) provide insights into the capacitive and diffusion contributions. Using these constants, the capacitive contribution percentage was calculated by eqn (5):[101]

$$\text{Capacitive contribution (\%)} = \frac{I_{\text{capacitive}}}{I_{\text{capacitive}} + I_{\text{diffusion}}} \times 100\% \quad (7)$$

The diffusion contribution can similarly be calculated by relation (eqn (8)):

$$\text{Diffusion contribution (\%)} = 100\% - \text{capacitive contribution (\%)} \quad (8)$$

In Fig. 9(a) is the trend of the capacitive and diffusion contributions as a function of scan rate. It is evident from the data that the capacitive contribution increases with increasing scan rate, highlighting the surface-controlled nature of the charge storage at higher scan rates. This trend is further supported by the curve in Fig. 9(b) and (c), which compares the CV profiles at 1 mV s^{-1} and 8 mV s^{-1}, respectively. At lower scan rates, diffusion-controlled processes dominate, as the ions have sufficient time to access the entire electrode surface. In contrast, at higher scan rates, the capacitive contribution increases as the process becomes more surface-controlled, resulting in faster ion exchange at the electrode–electrolyte interface.[101,102]

Furthermore, in Fig. 9(d) is the relationship between specific capacitance and scan rate. The Alv-ZnO NSs exhibit excellent specific capacitance at low scan rates, with values of 744.66 F g^{-1} at 1 mV s^{-1}, 701.9 F g^{-1} at 2 mV s^{-1}, 618.67 F g^{-1} at 5 mV s^{-1}, 558.42 F g^{-1} at 8 mV s^{-1}, 527.33 F g^{-1} at 10 mV s^{-1}, 441.67 F g^{-1} at 20 mV s^{-1}, 394.94 mV s^{-1} at 30 mV s^{-1}, 358.61 F g^{-1} at 40 mV s^{-1}, 326.27 F g^{-1} at 50 mV s^{-1}, and 292.36 F g^{-1} at 60 mV s^{-1}. The capacitance gradually decreases with increasing scan rates due to the limited accessibility of ions to the active sites at higher kinematics. Nevertheless, the high specific capacitance values and stable trend across the scan rates indicates the superior electrochemical performance of the material, further supported by the oxygen-rich surface attributed to the reducing and stabilizing effects of aloe vera gel.[5] The specific capacitance (F g^{-1}) was calculated from the CV data using the following eqn (9):[100]

$$C_{sp} = \frac{\int I \cdot \Delta v}{v \cdot m \cdot \Delta v} \quad (9)$$

where C_{sp} is the specific capacitance (F g^{-1}), I is the current (Amp), Δv is the potential window (Volt), v is the scan rate (V s^{-1}) and m is the active mass (gm).

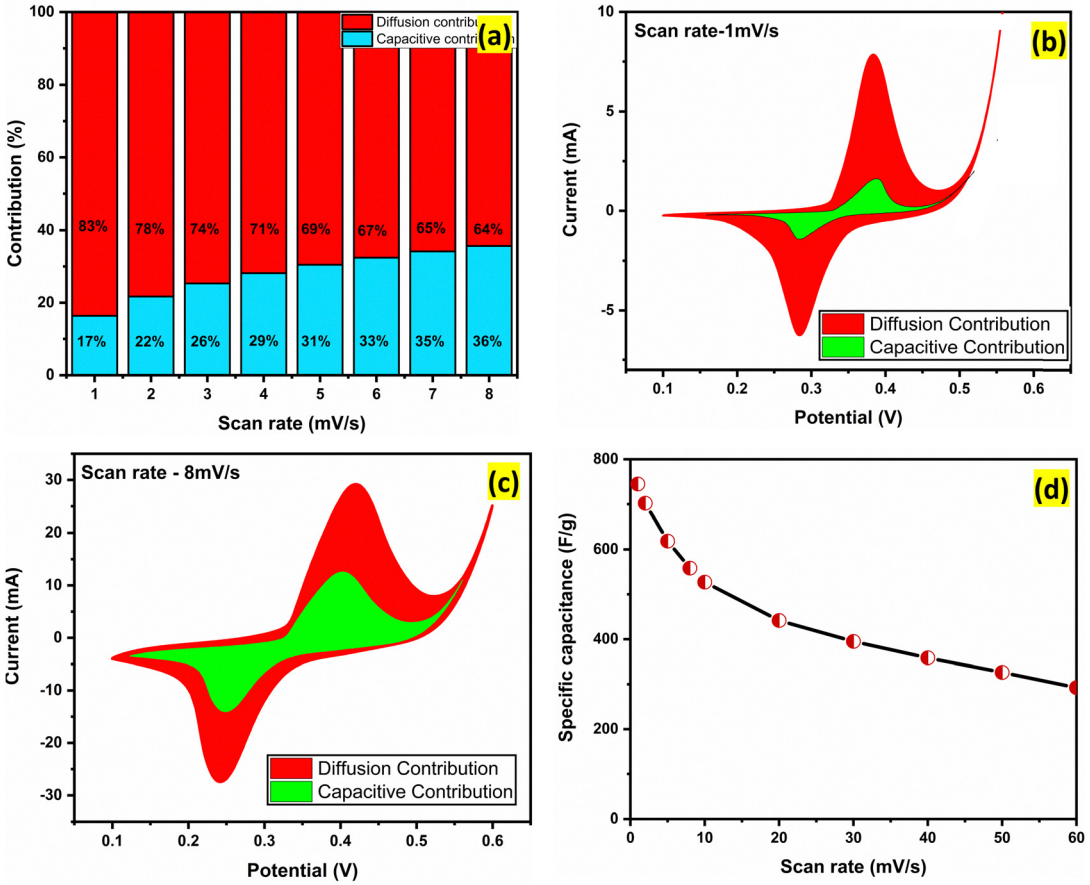

Fig. 9 (a) Bar diagram showing the capacitive and diffusion contributions to the overall current at varying scan rates. (b) and (c) CV profiles at 1 mV s^{-1} and 8 mV s^{-1} scan rates, illustrating the capacitive contribution at two different scan rates. (d) Specific capacitance *vs.* scan rate trend for the Alv-ZnO NSs, showing the variation in capacitance with changing scan rate.

The galvanostatic charge–discharge (GCD) behaviour of the Alv-ZnO NSs was evaluated at current densities ranging from 1 to 10 A g^{-1}, as shown in Fig. 10(a), to assess the performance of the material at different rates. The charge–discharge curves showed typical capacitive behaviour, with nearly symmetric shapes indicating excellent reversibility and fast ion transport within the electrode. The specific capacitance (C_{sp}) was calculated using eqn (10):[100]

$$C_{sp} = \frac{I_m \times \Delta t}{\Delta V} \quad (10)$$

where, I_m is the current density (A g^{-1}), Δt is the discharge time (s), and ΔV is the potential window (V).

At lower current densities (0.5, 1, and 2 A g^{-1}), the Alv-ZnO NSs exhibited higher specific capacitance, whereas at higher current densities (8 and 10 A g^{-1}), a slight decrease in capacitance was observed, which can be attributed to the limited diffusion of ions at faster charge–discharge rates. The specific capacitance values at different current densities were calculated to be 960 F g^{-1} at 0.5 A g^{-1}, 952.5 F g^{-1} at 1 A g^{-1}, 945 F g^{-1} at 2 A g^{-1}, 750 F g^{-1} at 5 A g^{-1}, 720 F g^{-1} at 8 A g^{-1}, and 700 F g^{-1} at 10 A g^{-1}. Notably, the capacitance at 10 A g^{-1} is 72.9% of that at 1 A g^{-1}, showing excellent material stability at higher current densities (Fig. 10(b)).

Furthermore, long-term cycling performance evaluated at a current density of 5 A g^{-1} demonstrated remarkable stability of the material, with 94.2% capacitance retention after 3000 charge–discharge cycles (Fig. 10(c)). The material also maintained a high coulombic efficiency of 93.5%, indicating excellent reversibility and consistent charge storage behavior throughout prolonged cycling. These values not only indicate good rate capability and stability across a wide range of operating conditions, but they also represent some of the highest specific capacitance values reported in the literature for SCs (Table 1), making Alv-ZnO NSs highly promising for practical SC applications.

To elucidate the mechanism behind the high electrochemical performance (952.5 F g^{-1} at 1 A g^{-1}), a detailed analysis of the defect-induced enhancement was undertaken. The Aloe vera-assisted synthesis facilitates the incorporation of intrinsic defects, primarily Zn vacancies and oxygen interstitials, as confirmed by both PL (Fig. 5(b), (c)) and XPS (Fig. 6(c), (d)) analyses. The PL spectrum displays multiple sub-bandgap emissions at ~3.38, 3.65, 3.42, 3.24, 3.16 and 3.10 eV, which align with transitions involving Zn and O lattice defects, as predicted by first-principle calculations and previously reported

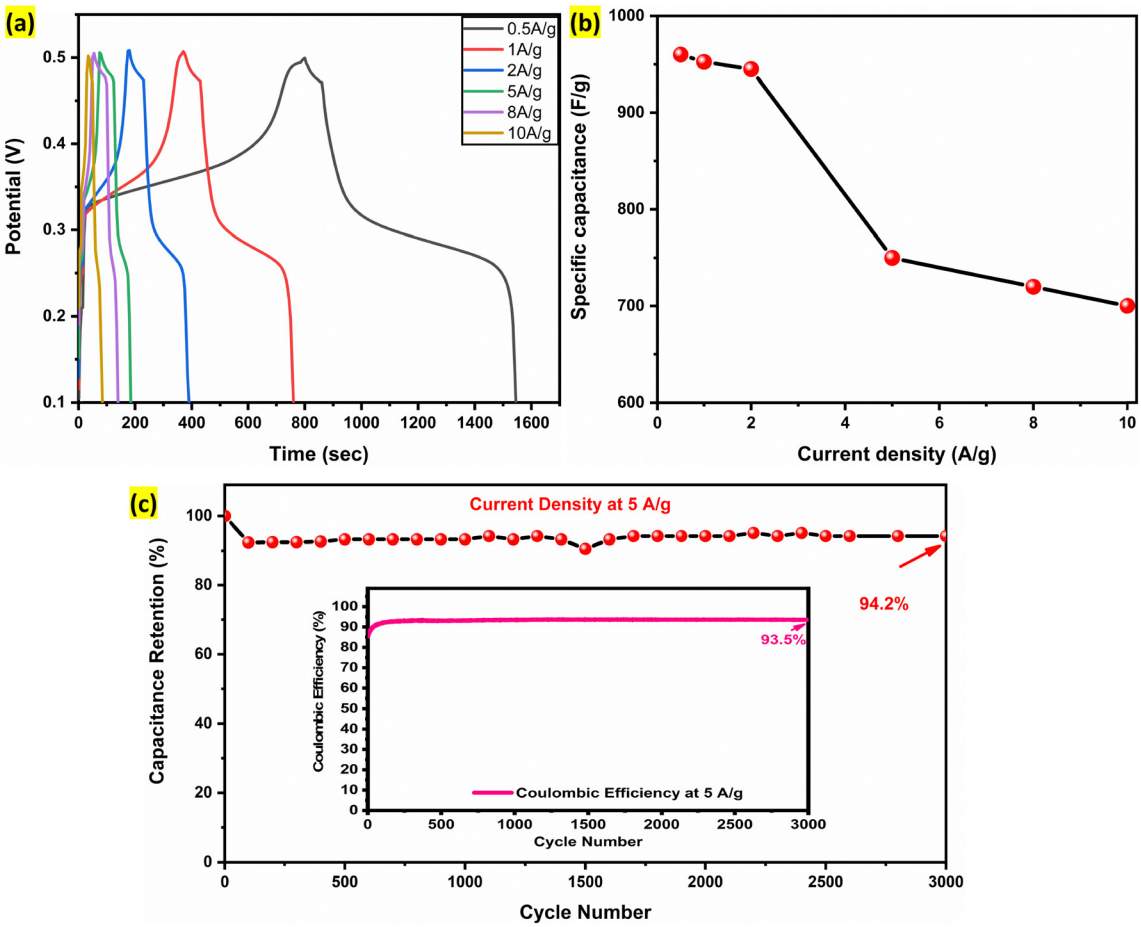

Fig. 10 (a) Charging and discharging behavior of the Alv-ZnO NSs, specific capacitance was calculated using eqn (10), with 1.5 mg of active material. (b) Variation of capacitance as a function of current density. (c) Cycling stability and coulombic efficiency at 5 A g^{-1} over 3000 charge–discharge cycles.

DFT studies.[76,78,83] Complementarily, XPS analysis reveals a blue shift in Zn $2p_{3/2}$ (~1023.2 eV) and O 1s (~532.0 eV) peaks, consistent with oxygen-rich surface states and Zn vacancies.[91] These defect sites act as redox-active centers, enabling rapid faradaic reactions at the electrode/electrolyte interface, thereby enhancing electrochemical performance. To quantitatively analyze the charge storage mechanism, cyclic voltammetry data were fitted using the power-law equation. The *b*-value derived from the anodic peak was 0.63 (Fig. 8(c)), indicating a mixed surface- and diffusion-controlled process typical of supercapattery-type storage.[58,100]. Furthermore, capacitive and diffusive contributions were separated using Dunn's model ($i(V) = k_1v + k_2v^{1/2}$), with the results plotted in Fig. 9(a)–(c). At lower scan rates (1–2 mV s^{-1}), diffusion dominates due to full electrolyte penetration; however, at higher scan rates (30–60 mV s^{-1}), the capacitive contribution rises above 65%, highlighting enhanced surface-controlled kinetics enabled by the defect-rich Alv-ZnO. These findings directly support the assertion that Aloe vera-induced defects play a central role in the electrochemical performance of the material.

Electrochemical impedance spectroscopy (EIS) was used to further investigate the charge transport properties of the Alv-ZnO NSs. The EIS data, shown in Fig. 11, reveal a solution resistance (R_S) of 0.56 Ω, which remained unchanged before and after the measurements, as seen in Fig. 11(a) and (b), respectively. However, the charge transfer resistance (R_{ct}) increased to 1.6 Ω after the experiments, indicating possible changes in the electrode/electrolyte interface. This suggests that the Alv-ZnO NSs maintain excellent conductivity while experiencing some interface modifications over cycling.

4. Conclusion

The aloe vera-assisted synthesis of ZnO nanostructures (Alv-ZnO NSs) successfully yielded highly crystalline and defect-engineered ZnO, demonstrating superior electrochemical properties for supercapattery applications. Rietveld refinement confirmed the high phase purity and structural integrity of the synthesized material. FESEM and HRTEM analysis revealed a well-defined needle-like nanostructure with a high surface area, ensuring efficient charge transport and electrolyte accessibility. PL and UV-vis spectroscopy established a bandgap of 3.74 ± 0.10 eV, with photoluminescence emissions confirming zinc vacancies and oxygen interstitials, which enhance charge storage capability. XPS analysis further validated these intrinsic defects, showing a blue shift in Zn 2p and O 1s peaks,

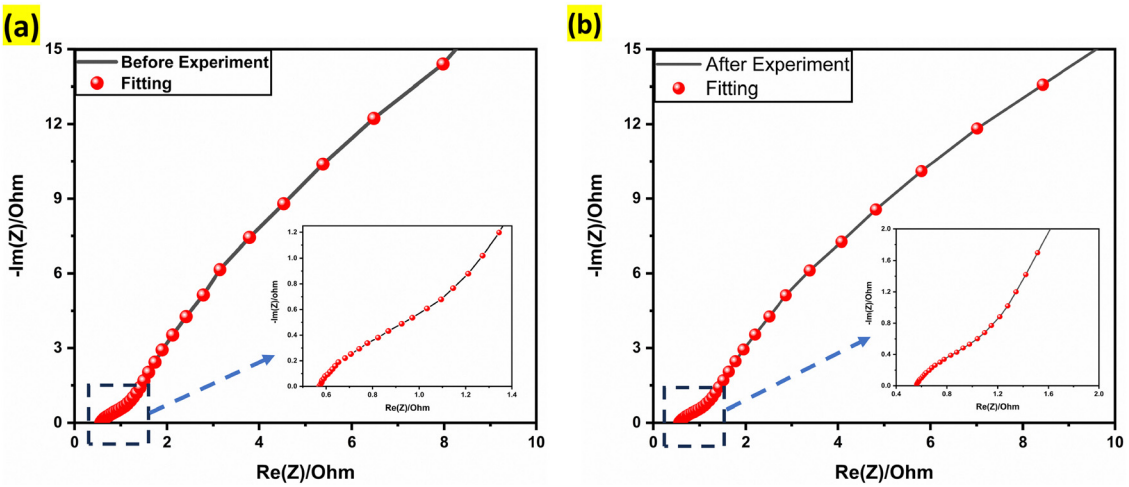

Fig. 11 (a) Nyquist plot showing EIS of the material before the experiment, and (b) Nyquist plot showing EIS after the experiment.

confirming an oxygen-rich surface favourable for redox activity. Electrochemical studies demonstrated an exceptional specific capacitance of 952.5 F g^{-1} at 1 A g^{-1} and 744.66 F g^{-1} at 1 mV s^{-1}, with 700 F g^{-1} at 10 A g^{-1}, indicating excellent rate capability. The capacitance retention of 72.9% from 1 A g^{-1} to 10 A g^{-1} highlights the stability of the material under high current densities. These findings, combined with excellent thermal stability, establish Alv-ZnO NSs as a sustainable, high-performance electrode material for supercapatteries. This study reinforces the potential of green synthesis in advancing next-generation energy storage technologies, offering an environmentally friendly and scalable solution for high-efficiency supercapatteries.

Author contributions

M. B.: conceptualization, investigation, data curation, formal analysis, methodology, visualization, writing – original draft. K. G.: conceptualization, methodology, formal analysis, writing – review & editing. A. V.: formal analysis. A. K. S.: supervision, project administration, writing – review & editing.

Conflicts of interest

The authors declare that they have no known competing financial interests or personal relationships that could have appeared to influence the work reported in this paper.

Data availability

The datasets generated during and/or analysed during the current study are not publicly available due to their inclusion in the author's ongoing PhD work but are available from the authors upon reasonable request.

Acknowledgements

The authors acknowledge CIC and R&D at UPES for providing the necessary research infrastructure. MB acknowledges BL-14, RRCAT, Indore, India for XPS characterization.

References

1 B. S. Sengar, V. Garg, A. Kumar, V. Awasthi, S. Kumar, V. V. Atuchin and S. Mukherjee, *Opt. Mater.*, 2018, **84**, 748–756.
2 V. P. Dragunov, V. Y. Dorzhiev, D. I. Ostertak and V. V. Atuchin, *Sens. Actuators, A*, 2018, **272**, 259–266.
3 C. Wu, T. Zhang, B. Ji, Y. Chou and X. Du, *Cellulose*, 2024, **31**, 4849–4864.
4 M. M. Sk, P. Pradhan, B. K. Patra and A. K. Guria, *Mater. Today Chem.*, 2023, **30**, 101582.
5 M. Bulla, V. Kumar, R. Devi, S. Kumar, A. K. Sisodiya, R. Dahiya and A. K. Mishra, *Sci. Rep.*, 2024, **14**, 7389.
6 S. Iravani, *Green Chem.*, 2011, **13**, 2638.
7 G. Scott, *Green Chem.*, 2014, **16**, 929.
8 C. Yuan, H. Xu, S. A. El-khodary, G. Ni, S. Esakkimuthu, S. Zhong and S. Wang, *Fuel*, 2024, **362**, 130795.
9 M. Czagany, S. Hompoth, A. K. Keshri, N. Pandit, I. Galambos, Z. Gacsi and P. Baumli, *Materials*, 2024, **17**, 702.
10 R. Liang, Y. Du, P. Xiao, J. Cheng, S. Yuan, Y. Chen, J. Yuan and J. Chen, *Nanomaterials*, 2021, **11**, 1248.
11 G. Manibalan, G. Murugadoss, P. Kuppusami, N. Kandhasamy and M. Rajesh Kumar, *J. Mater. Sci.: Mater. Electron.*, 2021, **32**, 5945–5954.
12 R. Arunachalam, R. K. V. Prataap, R. Pavul Raj, S. Mohan, J. Vijayakumar, L. Péter and M. Al Ahmad, *Surf. Eng.*, 2019, **35**, 102–108.
13 Y. Lu, B. Deng, Y. Liu, J. Wang, Z. Tu, J. Lu, X. Xiao and G. Xu, *Mater. Lett.*, 2021, **285**, 129101.

14 Y. Zhu, X. Ji, Z. Wu, W. Song, H. Hou, Z. Wu, X. He, Q. Chen and C. E. Banks, *J. Power Sources*, 2014, **267**, 888–900.
15 S. Sharma, P. Chand and S. Kaushik, *Sustainable Mater. Technol.*, 2024, **41**, e01045.
16 A. Manohar, V. Vijayakanth, S. V. P. Vattikuti, G. R. Reddy and K. H. Kim, *J. Energy Storage*, 2023, **68**, 107674.
17 S. Nandi, S. Kumar and A. Misra, *Mater. Adv.*, 2021, **2**, 6768–6799.
18 T. Wei, N. Zhang, Y. Ji, J. Zhang, Y. Zhu and T. Yi, *Chin. Chem. Lett.*, 2022, **33**, 714–729.
19 V. Garg, B. S. Sengar, V. Awasthi, A. Kumar, R. Singh, S. Kumar, C. Mukherjee, V. V. Atuchin and S. Mukherjee, *ACS Appl. Mater. Interfaces*, 2018, **10**, 5464–5474.
20 V. V. Atuchin, E. N. Galashov, A. S. Kozhukhov, L. D. Pokrovsky and V. N. Shlegel, *J. Cryst. Growth*, 2011, **318**, 1147–1150.
21 D. S. Abramkin, M. O. Petrushkov, D. B. Bogomolov, E. A. Emelyanov, M. Yu Yesin, A. V. Vasev, A. A. Bloshkin, E. S. Koptev, M. A. Putyato, V. V. Atuchin and V. V. Preobrazhenskii, *Nanomaterials*, 2023, **13**, 910.
22 K. Gautam, M. Bhatt, S. Dutt, A. Sagdeo and A. K. Sinha, *Sci. Rep.*, 2025, **15**, 11506.
23 M. Mahajan, S. Kumar, J. Gaur, S. Kaushal, J. Dalal, G. Singh, M. Misra and D. S. Ahlawat, *RSC Adv.*, 2025, **15**, 2958–2980.
24 H. Kaur, A. Sharma, K. Anand, A. Panday, S. Tagotra, S. Kakran, A. K. Singh, M. W. Alam, S. Kumar, G. Bouzid, J. Dalal and G. Singh, *RSC Adv.*, 2025, **15**, 16742–16765.
25 A. Raza, K. Sayeed, A. Naaz, M. Muaz, S. N. Islam, S. Rahaman, F. Sama, K. Pandey and A. Ahmad, *ACS Omega*, 2024, **9**(30), 32444–32454, DOI: **10.1021/acsomega.3c10060**.
26 I. Shaheen, K. S. Ahmad, C. Zequine, R. K. Gupta, A. G. Thomas and M. A. Malik, *RSC Adv.*, 2021, **11**, 23374–23384.
27 N. Ansar, W. Shahid, M. A. Irshad, S. Shahid, R. Nawaz, A. Irfan, M. I. Khan, A. A. Al-Mutairi, M. Khizar, S. A. Al-Hussain, S. Ullah and M. E. A. Zaki, *Sci. Rep.*, 2024, **14**, 12711.
28 Q. N. Tran, C. H. Park, L. Sang-Wha and V. A. Tran, *Mater. Today Chem.*, 2025, **46**, 102721.
29 V. K. Hoang Bui, M. K. Kumar, M. Alinaghibeigi, S. Moolayadukkam, S. Eskandarinejad, S. Mahmoudi, S. Mirzamohammadi and M. Rezaei-khamseh, *J. Compos. Compd.*, 2021, **3**, 182–193.
30 D. A. Tonpe, K. P. Gattu, V. V. Kutwade, S.-H. Han, B. R. Sathe and R. Sharma, *J. Energy Storage*, 2024, **81**, 110434.
31 H. Cheng, G. Xu, C. Zhu, Z. Alhalili, X. Du and G. Gao, *Chem. Eng. J.*, 2023, **454**, 140454.
32 X. Shi, S. Liu, B. Tang, X. Lin, A. Li, X. Chen, J. Zhou, Z. Ma and H. Song, *Chem. Eng. J.*, 2017, **330**, 453–461.
33 S. Vennila, C. Leelavathi, V. Balaprakash, K. Thangavel, S. A. Kumar, J. K. Sundar and R. Ramesh, *J. Mater. Sci.: Mater. Electron.*, 2025, **36**, 489.
34 H. N. Abdelhamid, S. A. Al Kiey and W. Sharmoukh, *Appl. Organomet. Chem.*, 2022, **36**, e6486.
35 X. Zheng, X. Yan, Y. Sun, Z. Bai, G. Zhang, Y. Shen, Q. Liang and Y. Zhang, *ACS Appl. Mater. Interfaces*, 2015, **7**, 2480–2485.
36 X. Sun, Q. Li, Y. Lü and Y. Mao, *Chem. Commun.*, 2013, **49**, 4456.
37 P. Yang, X. Xiao, Y. Li, Y. Ding, P. Qiang, X. Tan, W. Mai, Z. Lin, W. Wu, T. Li, H. Jin, P. Liu, J. Zhou, C. P. Wong and Z. L. Wang, *ACS Nano*, 2013, **7**, 2617–2626.
38 S. Li, J. Wen, X. Mo, H. Long, H. Wang, J. Wang and G. Fang, *J. Power Sources*, 2014, **256**, 206–211.
39 J. Salamon, A. Simi, H. J. Prabu, A. F. Sahayaraj, A. J. S. Kennedy and I. Johnson, *J. Inorg. Organomet. Polym.*, 2025, **35**, 342–355.
40 C. Sasirekha, S. Arumugam and G. Muralidharan, *Appl. Surf. Sci.*, 2018, **449**, 521–527.
41 S. Chakraborty, A. R. M and N. L. Mary, *J. Energy Storage*, 2020, **28**, 101275.
42 H. Bishwakarma, R. Tyagi, N. Kumar and A. K. Das, *Environ. Res.*, 2023, **218**, 115021.
43 J. Meena, G. Pavithra, D. Anusha, A. S. Kumar and K. Santhakumar, *J. Mater. Sci.: Mater. Electron.*, 2023, **34**, 1131.
44 K. Rajangam, K. S. Gowri, R. P. Kumar, L. M. Surriya, S. V. Raj, B. Balraj and S. Thangavel, *Mater. Res. Express*, 2019, **6**, 095524.
45 Y. Haldorai, W. Voit and J.-J. Shim, *Electrochim. Acta*, 2014, **120**, 65–72.
46 E. R. Ezeigwe, M. T. T. Tan, P. S. Khiew and C. W. Siong, *Ceram. Int.*, 2015, **41**, 715–724.
47 X. Xiao, B. Han, G. Chen, L. Wang and Y. Wang, *Sci. Rep.*, 2017, **7**, 40167.
48 Y. Zhang, X. Sun, L. Pan, H. Li, Z. Sun, C. Sun and B. K. Tay, *Solid State Ionics*, 2009, **180**, 1525–1528.
49 D. Kalpana, K. S. Omkumar, S. S. Kumar and N. G. Renganathan, *Electrochim. Acta*, 2006, **52**, 1309–1315.
50 M. Selvakumar, D. Krishna Bhat, A. Manish Aggarwal, S. Prahladh Iyer and G. Sravani, *Phys. B*, 2010, **405**, 2286–2289.
51 D. Kalpana, K. S. Omkumar, S. S. Kumar and N. G. Renganathan, *Electrochim. Acta*, 2006, **52**, 1309–1315.
52 R. D. Kumar, S. Nagarani, S. Balachandran, C. Brundha, S. H. Kumar, R. Manigandan, M. Kumar, V. Sethuraman and S. H. Kim, *Surf. Interfaces*, 2022, **33**, 102203.
53 M. Saranya, R. Ramachandran and F. Wang, *J. Sci.: Adv. Mater. Devices*, 2016, **1**, 454–460.
54 C. Lefdhil, S. Polat and H. Zengin, *Nanomaterials*, 2023, **13**, 2423.
55 F. Ahmed, G. Almutairi, B. AlOtaibi, S. Kumar, N. Arshi, S. G. Hussain, A. Umar, N. Ahmad and A. Aljaafari, *Nanomaterials*, 2020, **10**, 1979.
56 K. K. Purushothaman, V. Suba Priya, S. Nagamuthu, S. Vijayakumar and G. Muralidharan, *Micro Nano Lett.*, 2011, **6**, 668–670.
57 S. Najib, F. Bakan, N. Abdullayeva, R. Bahariqushchi, S. Kasap, G. Franzò, M. Sankir, N. Demirci Sankir, S. Mirabella and E. Erdem, *Nanoscale*, 2020, **12**, 16162–16172.

58 M. Bhatt, B. Gupta and A. K. Sinha, *Sci. Rep.*, 2025, **15**, 2192.
59 T. Ramkumar, M. Selvakumar, R. Vasanthsankar, A. S. Sathishkumar, P. Narayanasamy and G. Girija, *J. Magnesium Alloys*, 2018, **6**, 390–398.
60 K. Pradeeswari, A. Venkatesan, P. Pandi, K. Karthik, K. V. Hari Krishna and R. Mohan Kumar, *Mater. Res. Express*, 2019, **6**, 105525.
61 W. Chen, X. Liu, Y. Liu and H.-I. Kim, *Colloid Polym. Sci.*, 2010, **288**, 1393–1399.
62 A. Awad, A. I. Abou-Kandil, I. Elsabbagh, M. Elfass, M. Gaafar and E. Mwafy, *J. Thermoplast. Compos. Mater.*, 2015, **28**, 1343–1358.
63 M. Chelu, M. Popa, E. A. Ozon, J. Pandele Cusu, M. Anastasescu, V. A. Surdu, J. Calderon Moreno and A. M. Musuc, *Polymers*, 2023, **15**, 1312.
64 N. N. Golovnev, M. S. Molokeev, S. N. Vereshchagin, V. V. Atuchin, M. Y. Sidorenko and M. S. Dmitrushkov, *Polyhedron*, 2014, **70**, 71–76.
65 N. N. Golovnev, M. S. Molokeev, S. N. Vereshchagin and V. V. Atuchin, *J. Coord. Chem.*, 2015, **68**, 1865–1877.
66 Y. G. Denisenko, V. V. Atuchin, M. S. Molokeev, A. E. Sedykh, N. A. Khritokhin, A. S. Aleksandrovsky, A. S. Oreshonkov, N. P. Shestakov, S. V. Adichtchev, A. M. Pugachev, E. I. Sal'nikova, O. V. Andreev, I. A. Razumkova and K. Müller-Buschbaum, *Molecules*, 2022, **27**, 3966.
67 V. B. Platonov, M. N. Rumyantseva, A. S. Frolov, A. D. Yapryntsev and A. M. Gaskov, *Beilstein J. Nanotechnol.*, 2019, **10**, 1537–1547.
68 K. M. Mohamed, J. J. Benitto, J. J. Vijaya and M. Bououdina, *Crystals*, 2023, **13**, 329.
69 V. V. Atuchin, T. A. Gavrilova, V. G. Kostrovsky, L. D. Pokrovsky and I. B. Troitskaia, *Inorg. Mater.*, 2008, **44**, 622–627.
70 N. I. Rasli, H. Basri and Z. Harun, *Heliyon*, 2020, **6**, e03156.
71 M. Bhatt, A. K. Sinha, P. Bhojane, M. N. Singh and M. Gupta, *J. Mater. Sci.: Mater. Electron.*, 2023, **34**, 1933.
72 Z. M. Almarhoon, T. Indumathi and E. R. Kumar, *J. Mater. Sci.: Mater. Electron.*, 2022, **33**, 23659–23672.
73 A. R. Kachere, P. M. Kakade, A. R. Kanwade, P. Dani, N. T. Mandlik, S. R. Rondiya, N. Y. Dzade, S. R. Jadkar and S. V. Bhosale, *ES Mater. Manuf.*, 2022, **16**, 19–29, DOI: 10.30919/esmm5f516.
74 S. Chandran, J. C. Sunny, S. Chandran and C. Bellan, *Mater. Today: Proc.*, 2018, **5**, 16190–16198.
75 L. Ma, Z. Xia, V. Atuchin, M. Molokeev, S. Auluck, A. H. Reshak and Q. Liu, *Phys. Chem. Chem. Phys.*, 2015, **17**, 31188–31194.
76 B. Lin, Z. Fu and Y. Jia, *Appl. Phys. Lett.*, 2001, **79**, 943–945.
77 S. A. M. Lima, F. A. Sigoli, M. Jafelicci Jr and M. R. Davolos, *Int. J. Inorg. Mater.*, 2001, **3**, 749–754.
78 P. S. Xu, Y. M. Sun, C. S. Shi, F. Q. Xu and H. B. Pan, *Nucl. Instrum. Methods Phys. Res., Sect. B*, 2003, **199**, 286–290.
79 J. Wang, Z. Wang, B. Huang, Y. Ma, Y. Liu, X. Qin, X. Zhang and Y. Dai, *ACS Appl. Mater. Interfaces*, 2012, **4**, 4024–4030.
80 V. V. Atuchin, L. I. Isaenko, V. G. Kesler, Z. S. Lin, M. S. Molokeev, A. P. Yelisseyev and S. A. Zhurkov, *J. Solid State Chem.*, 2012, **187**, 159–164.
81 A. H. Reshak, Z. A. Alahmed, J. Bila, V. V. Atuchin, B. G. Bazarov, O. D. Chimitova, M. S. Molokeev, I. P. Prosvirin and A. P. Yelisseyev, *J. Phys. Chem. C*, 2016, **120**, 10559–10568.
82 M. Nabil, I. V. Perez-Quintana, M. Acosta, J. A. Mendez-Gamboa and R. Castro-Rodriguez, *Adv. Mater. Sci. Eng.*, 2021, **2021**, 9926544.
83 A. B. Djurišić and Y. H. Leung, *Small*, 2006, **2**, 944–961.
84 M. Stefan, A. M. Rostas, A. U. Ammar, A. Güngör, E. Saritas, D. Toloman, A. Varadi, S. Macavei, L. Barbu-Tudoran, C. Leostean, O. Pana, A. Kasza, E. Erdem and A. Popa, *Energy Fuels*, 2024, **38**, 19088–19099.
85 R. Rathnasekara, G. Mayberry and P. Hari, *Materials*, 2022, **15**, 8816.
86 F. Kayaci, S. Vempati, I. Donmez, N. Biyikli and T. Uyar, *Nanoscale*, 2014, **6**, 10224–10234.
87 M. I. Torres-Ramos, U. J. Martín-Camacho, J. L. González, M. F. Yañez-Acosta, L. Becerra-Solano, Y. K. Gutiérrez-Mercado, M. Macias-Carballo, C. M. Gómez, O. A. González-Vargas, J. A. Rivera-Mayorga and A. Pérez-Larios, *Int. J. Mol. Sci.*, 2022, **23**, 7258.
88 C. V. Ramana, R. S. Vemuri, V. V. Kaichev, V. A. Kochubey, A. A. Saraev and V. V. Atuchin, *ACS Appl. Mater. Interfaces*, 2011, **3**, 4370–4373.
89 D. Fang, F. He, J. Xie and L. Xue, *J. Wuhan Univ. Technol., Mater. Sci. Ed.*, 2020, **35**, 711–718.
90 V. V. Atuchin, E. N. Galashov, O. Yu Khyzhun, A. S. Kozhukhov, L. D. Pokrovsky and V. N. Shlegel, *Cryst. Growth Des.*, 2011, **11**, 2479–2484.
91 M. Claros, M. Setka, Y. P. Jimenez and S. Vallejos, *Nanomaterials*, 2020, **10**, 471.
92 R. Al-Gaashani, S. Radiman, A. R. Daud, N. Tabet and Y. Al-Douri, *Ceram. Int.*, 2013, **39**, 2283–2292.
93 A. Sahai and N. Goswami, *Ceram. Int.*, 2014, **40**, 14569–14578.
94 V. V. Atuchin, I. E. Kalabin, V. G. Kesler and N. V. Pervukhina, *J. Electron Spectrosc. Relat. Phenom.*, 2005, **142**, 129–134.
95 C. V. Ramana, V. V. Atuchin, V. G. Kesler, V. A. Kochubey, L. D. Pokrovsky, V. Shutthanandan, U. Becker and R. C. Ewing, *Appl. Surf. Sci.*, 2007, **253**, 5368–5374.
96 V. V. Atuchin, E. N. Galashov, O. Yu Khyzhun, A. S. Kozhukhov, L. D. Pokrovsky and V. N. Shlegel, *Cryst. Growth Des.*, 2011, **11**, 2479–2484.
97 V. V. Atuchin, J.-C. Grivel, A. S. Korotkov and Z. Zhang, *J. Solid State Chem.*, 2008, **181**, 1285–1291.
98 E. J. Rubio, V. V. Atuchin, V. N. Kruchinin, L. D. Pokrovsky, I. P. Prosvirin and C. V. Ramana, *J. Phys. Chem. C*, 2014, **118**, 13644–13651.
99 N. Poompiew, P. Pattananuwat and P. Potiyaraj, *ACS Omega*, 2021, **6**, 25138–25150.
100 S. Kumar, B. K. Satpathy and D. Pradhan, *Mater. Adv.*, 2024, **5**, 2271–2284.
101 Y. Lan, H. Zhao, Y. Zong, X. Li, Y. Sun, J. Feng, Y. Wang, X. Zheng and Y. Du, *Nanoscale*, 2018, **10**, 11775–11781.
102 H. Su, T. Xiong, Q. Tan, F. Yang, P. B. S. Appadurai, A. A. Afuwape, M.-S. Jie, T. Balogun, Y. Huang and K. Guo, *Nanomaterials*, 2020, **10**, 1141.